
Neuronal Self-Adaptation Enhances Capacity and Robustness of Representation in Spiking Neural Networks

Zhuobin Yang¹ Yeyao Bao¹ Liangfu Lv¹ Jian Zhang¹ Xiaohong Li¹ Yunliang Zang¹

Abstract

Spiking Neural Networks (SNNs) are promising for energy-efficient, real-time edge computing, yet their performance is often constrained by the limited adaptability of conventional leaky integrate-and-fire (LIF) neurons. Existing LIF models struggle with restricted information capacity and susceptibility to noise, leading to degraded accuracy and compromised robustness. Inspired by the dynamic self-regulation of biological potassium channels, we propose the Potassium-regulated LIF (KvLIF) neuron model. KvLIF introduces an auxiliary conductance state that integrates membrane potential and spiking history to adaptively modulate neuronal excitability and reset dynamics. This design extends the dynamic response range of neurons to varying input intensities and effectively suppresses noise-induced spikes. We extensively evaluate KvLIF on both static image and neuromorphic datasets, demonstrating consistent improvements in classification accuracy and superior robustness compared to existing LIF models. Our work bridges biological plausibility with computational efficiency, offering a neuron model that enhances SNN performance while maintaining suitability for low-power neuromorphic deployment.

1. Introduction

Spiking Neural Networks (SNNs) offer biological plausibility, event-driven computation, and strong spatio-temporal processing, with significant energy efficiency on neuromorphic hardware for low-power, real-time applications (Maass, 1997; Gerstner & Kistler, 2002; Schuman et al., 2022). The Leaky Integrate-and-Fire (LIF) neuron model is a core component for its simplicity and biological relevance (Gerstner et al., 2014). but its non-differentiable spiking hinders direct

backpropagation, motivating surrogate gradient (SG) methods (Wu et al., 2018; Zenke & Ganguli, 2018). Membrane potential reset plays a key role in performance: soft reset preserves residual temporal information, while hard reset discards it (Wu et al., 2018; Guo et al., 2022). Although soft reset is generally advantageous in preserving temporal information, conventional LIF models still face limitations that constrain their effectiveness in complex temporal tasks.

In SNNs, input signals are typically encoded into spike trains whose firing rates depend on input intensity (Eshraghian et al., 2023). Under varying intensities (e.g., changes in image brightness or contrast), conventional LIF neurons operate within a fixed and narrow sensitivity range, limiting their ability to adapt and potentially hindering overall SNN performance. For high-intensity inputs (see examples in Figure 5, Appendix A), both hard and soft reset models saturate at their maximum firing rates under the current SNN simulation configuration (Figure 1(a)). Consequently, they produce identical outputs and fail to differentiate between input levels in the upper range. The limited dynamic range of conventional LIF neurons constrains fine-grained information encoding. Apart from the incapability of distinguishing high intensity input, in scenarios involving temporally rich data, soft reset mechanism introduces an additional problem: noise inputs occurring after an event-triggered spike can falsely initiate another spike, leading to false-positive event detections (Figure 1(b)). These limitations underscore the necessity for a neuronal mechanism that can adaptively broaden the dynamic response range and effectively suppress noise-induced spikes.

Although LIF models resemble neuronal spiking, biological neurons exhibit more dynamic spiking responses due to the influence of diverse biological factors. In particular, neurons contain diverse ion currents that enable self-adaptive behavior under varying input signal intensities (Zang et al., 2023; Benda & Herz, 2003). Even within the same type of ion channel, different components can exhibit distinct properties. As shown in Figure 2(a), A-type potassium currents activate within the subthreshold potential range, dampening neuronal excitability to prevent premature action potential generation (Bean, 2007). In contrast, components like delayed-rectifier potassium currents activate only at

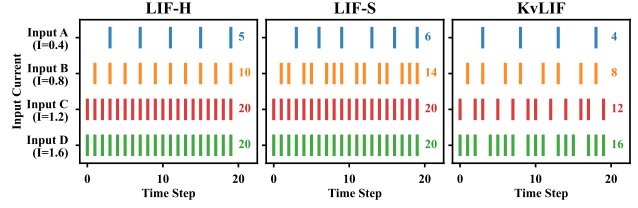
¹Academy of Medical Engineering and Translational Medicine, Tianjin University, Tianjin, China. Correspondence to: Yunliang Zang <yunliangzang@tju.edu.cn>.

higher membrane potentials, primarily driving membrane repolarization and contributing to the subsequent afterhyperpolarization (Zang et al., 2020). These ion channels can modulate their activation and deactivation states based on real-time membrane potential and spiking experience, thereby dynamically adjusting a neuron’s response range and contributing to working memory (Fitz et al., 2020).

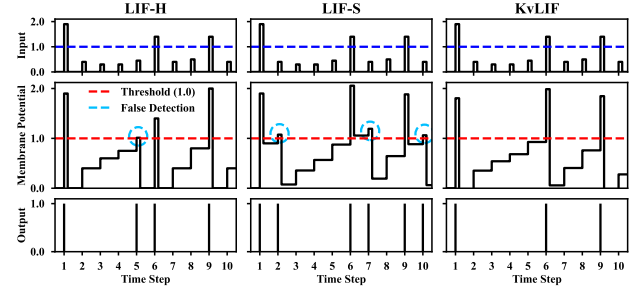
In this work, inspired by the adaptive neuronal responses, we propose a biologically plausible Potassium Regulated Leaky Integrate-and-Fire (KvLIF) model. By dynamically adjusting its sensitivity range based on spiking history and real-time membrane potential, KvLIF achieves robust spike encoding across a wide range of input intensities in static signals and reduces spurious event detections in temporally rich data (Figure 1). The KvLIF model introduces an auxiliary state variable, $K[t]$, representing the total potassium conductance of the neuron. This variable integrates historical membrane potential fluctuations and spiking activity to adaptively modulate neuronal excitability. During the sub-threshold phase, $K[t]$ mimics A-type potassium channels by imposing voltage-dependent input shunting, suppressing membrane depolarization. Upon spike generation, $K[t]$ emulates delayed rectifier potassium channels by driving a dynamic voltage reset mechanism that reproduces the biological after-hyperpolarization effect. Together, $K[t]$ incorporates both membrane potential and spiking experience into the model to adjust neuronal response. This design provides several computational benefits: extended dynamic range, noise robustness, and shorter inference windows, when compared to the conventional LIF models.

The main contributions of this work are as follows:

- **Analysis of LIF model limitations:** We provide a detailed investigation of the fundamental limitations of conventional LIF neuron models, including restricted response ranges and vulnerability to noise.
- **A biologically inspired adaptive neuron:** Motivated by the self-regulatory mechanisms in biological neurons, we propose the KvLIF model, which incorporates a dynamic regulatory state governed by membrane potential fluctuations and spiking history. This design enables a more flexible response profile and enhanced robustness.
- **Comprehensive empirical validation:** We perform extensive experiments across both static and neuromorphic datasets, demonstrating that the proposed KvLIF model consistently surpasses existing neuron models in classification accuracy and robustness to noises.



(a) Neuronal responses to varying input intensities.



(b) Neuronal responses to temporal input.

Figure 1. Simulation comparison of the KvLIF model and conventional LIF variants regarding dynamic response range and noise robustness. LIF-S: LIF model with soft reset; LIF-H: LIF model with hard reset.

2. Related Work

2.1. Parametric Optimizations of Spiking Neurons

Conventional LIF neurons, while computationally efficient, often struggle to capture complex spatiotemporal dynamics. Optimizing the internal parameters of neurons is an effective method for processing multi-scale temporal information. The PLIF model introduces learnable membrane time constants, enabling the network to adapt its integration dynamics through gradient-based training (Fang et al., 2021). Similarly, LTMD incorporates learnable spiking thresholds, allowing neurons to adjust their firing sensitivity (Wang et al., 2022). Expanding the parameter space with additional structured parameters represents another viable strategy. For example, GLIF integrates learnable gating factors that combine diverse biological features, providing flexible control over information flow (Yao et al., 2022). Likewise, TC-LIF employs a two-compartment architecture with specific coupling parameters to enhance the modeling of long-term temporal dependencies (Zhang et al., 2024).

However, despite the significant improvements in representational capability offered by these parametric methods, neuronal dynamics remain fixed once training is complete—i.e., static during inference (Wang & Yu, 2024). This contrasts with the adaptive capability inherent in biological neurons, underscoring a key opportunity to improve model adaptability and robustness in complex dynamic environments.

2.2. Adaptation Mechanisms in Spiking Neurons

Various dynamic adaptation mechanisms have proven effective in enhancing network representational capability and gradient propagation efficiency.

To mitigate the gradient vanishing problem, Huang et al. propose the CLIF neuron model (Huang et al., 2024), which introduces a complementary membrane potential to create additional backpropagation pathways and effectively retain temporal gradients. Similarly, the ILIF model employs an adaptive inhibition mechanism by introducing two independent inhibitory variables to balance gradient preservation and neuronal overactivation (Sun et al., 2025). Focusing on information retention, Huang et al. design the AR-LIF model, which uses an adaptive reset strategy and dynamic thresholds to reduce information loss associated with traditional reset modes (Huang et al., 2025). Furthermore, to capture complex spatio-temporal dependencies, Wang et al. present the STC-LIF model, incorporating learnable autaptic circuits that dynamically regulate input and historical information, thereby enhancing the network’s predictive capabilities (Wang & Yu, 2024).

While these approaches effectively enhance network trainability and representation capabilities through adaptive mechanisms, they primarily focus on facilitating gradient propagation and optimizing learning dynamics. In contrast, the proposed KvLIF model targets the neuron’s intrinsic self-adaptation motivated by biological potassium currents. By integrating potassium conductance dynamics, the KvLIF expands the dynamic response range, suppresses noise-induced spikes, and reduces the required inference time window. Moreover, KvLIF outperforms these models across metrics that evaluate these capabilities.

3. Preliminary

3.1. LIF Neuron Model

The LIF model serves as the foundational computational unit in SNNs. As shown in Figure 2(b), the LIF neuron maintains an internal membrane potential that evolves over time. The subthreshold dynamics for neurons in layer l at time step t are governed by the accumulation of postsynaptic current $I^l[t]$ and the decay of their previous membrane potential $U^l[t-1]$. The membrane potential update is expressed as:

$$I^l[t] = W^l S^{l-1}[t] \quad (1)$$

$$U^l[t] = \lambda U^l[t-1] + I^l[t] \quad (2)$$

Here, $\lambda \in (0, 1)$ is the membrane decay constant, and W^l denotes the synaptic weights from layer $l-1$ to layer l . $S^{l-1}[t]$ represents the spikes of layer $l-1$ neurons at time step t .

Nonlinearity is introduced via a spike generation mechanism. The binary output $S^l[t]$ is generated by Heaviside function $H(\cdot)$ when the accumulated potential $U^l[t]$ exceeds the firing threshold V_{th} . The mathematical expression as shown in Eq.(3):

$$S^l[t] = H(U^l[t] - V_{th}) = \begin{cases} 1, & U^l[t] \geq V_{th} \\ 0, & otherwise \end{cases} \quad (3)$$

After spiking, neurons reset their membrane potentials to prepare for the next firing. This process is illustrated in Eq.(4):

$$U^l[t] = \begin{cases} U^l[t] - V_{th} S^l[t], & \text{soft reset} \\ U^l[t] \odot (1 - S^l[t]), & \text{hard reset} \end{cases} \quad (4)$$

Here, \odot denotes the element-wise multiplication.

3.2. SNN Training Framework

The training process relies on the Backpropagation Through Time (BPTT) algorithm (Werbos, 2002). To capture temporal dynamics, the gradients for the synaptic weights W^l are calculated by accumulating the derivatives of the loss function L across all time steps T :

$$\nabla_{W^l} L = \sum_{t=1}^T \frac{\partial L}{\partial U^l[t]} \frac{\partial U^l[t]}{\partial W^l} \quad (5)$$

To facilitate the backward flow of gradients through the non-differentiable spiking mechanism, the framework incorporates the SG strategy. In this work, the derivative of the spike generation function is approximated using a rectangular function $\mathbb{H}(\cdot)$:

$$\frac{\partial S^l[t]}{\partial U^l[t]} \approx \mathbb{H}(U^l[t]) = \frac{1}{\sigma} \cdot \mathbb{I}(|U^l[t] - V_{th}| < \frac{\sigma}{2}) \quad (6)$$

where $\mathbb{I}(\cdot)$ denotes the indicator function, and σ serves as a hyperparameter typically set to the threshold value V_{th} .

3.3. Voltage-gated Potassium Currents

Voltage-gated potassium channels are key intrinsic regulators of neuronal excitability. In particular, the A-type potassium current is recruited during the subthreshold depolarization phase. It generates an outward current that shunts excitatory inputs to delay spike initiation and regulate firing frequency (Connor & Stevens, 1971). After spiking, the delayed rectifier potassium channels dominate the repolarization phase. This current facilitates the restoration of the resting membrane potential and determines the depth of afterhyperpolarization (Bean, 2007). Such coordinated dynamic regulation prevents stochastic firing and is critical for maintaining network stability (Vacher et al., 2008).

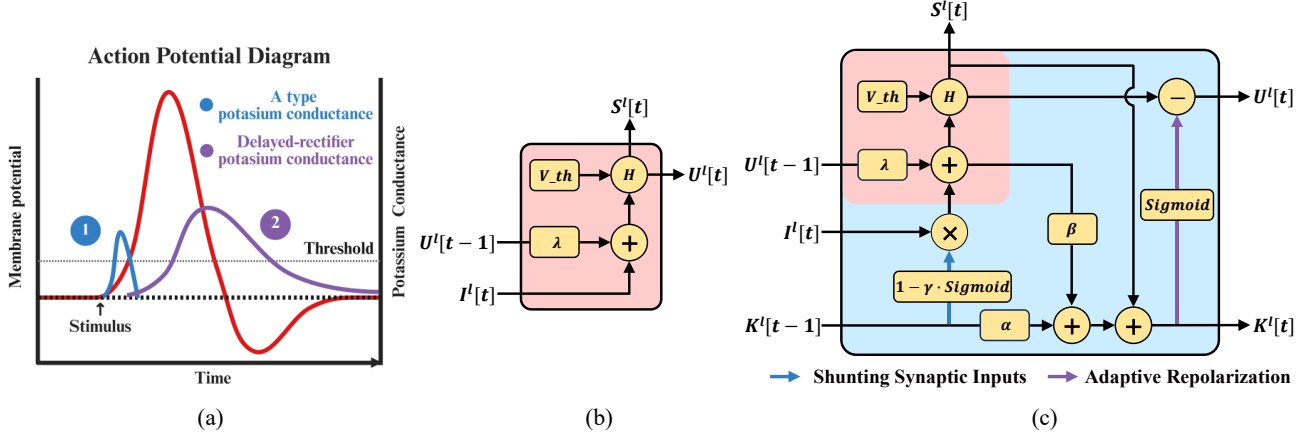


Figure 2. (a) Schematic of biological action potential regulation involving two distinct potassium channel subtypes. (b) Computational flow of the LIF model with soft reset. (c) Computational flow of the proposed KvLIF model.

4. Methodology

4.1. Limitation of LIF Neuron Model

For the LIF neuron model with soft reset, when a neuron fires at time step $t - 1$ with a membrane potential $U[t - 1]$ exceeding the threshold V_{th} , the residual potential $\delta[t - 1]$ retained after the soft reset is calculated as:

$$\delta[t - 1] = U[t - 1] - V_{th} \quad (7)$$

where $\delta[t - 1] > 0$. According to the Eq.(2), the condition for generating a consecutive spike at time step t can be rewritten as:

$$\lambda\delta[t - 1] + I[t] > V_{th} \quad (8)$$

Solving for the input current $I[t]$, we derive the minimum input current required to generate a spike, denoted as $I_{min}^{soft}[t]$:

$$I_{min}^{soft}[t] = V_{th} - \lambda\delta[t - 1] \quad (9)$$

Given $0 < \lambda < 1$ and $\delta[t - 1] > 0$, it strictly holds that $I_{min}[t] < V_{th}$. This inequality mathematically proves that the retention of $\delta[t - 1]$ lowers the firing threshold, rendering the model more sensitive to subsequent inputs.

Furthermore, this inertia effect is exacerbated during continuous firing sequences. Consider a scenario where the neuron fires continuously over time steps $t = 1, \dots, T$, driven by a constant input overload $\Delta I = I - V_{th} > 0$. The residual potential $\delta[T]$ accumulates recursively. By expanding the recursion $\delta[T] = \lambda\delta[T] + \Delta I$ from an initial state $\delta[0] = 0$, we obtain a geometric series:

$$\delta[T] = \Delta I \sum_{i=0}^{T-1} \lambda^i = \Delta I \frac{1 - \lambda^T}{1 - \lambda} \quad (10)$$

We now examine the minimum input required for the next spike at $t = T + 1$, which is $I_{min}^{soft}[T + 1] = V_{th} - \lambda\delta[T]$.

Since $\delta[T]$ increases monotonically with T , the minimum input current required for the next spike at $t = T + 1$ decreases:

$$I_{min}^{soft}[T + 1] < I_{min}^{soft}[T] \quad (11)$$

This demonstrates the cumulative inertia inherent in models with soft reset: continuous spiking monotonically reduces the threshold required to sustain firing. This phenomenon not only progressively diminishes the model's ability to discriminate different input intensities, but also increases its sensitivity to noise.

In the hard-reset LIF model, the membrane potential is forced to zero immediately after spiking. Although this prevents cumulative inertia, it also eliminates the residual potential, hindering the retention of historical activity information and resulting in a limited dynamic response range.

4.2. The Design of KvLIF Model

Inspired by the biophysical dynamics of voltage-gated potassium channels that regulate neuronal excitability, repolarization and accommodation, we propose the KvLIF model. As shown in Figure 2(c), the model includes a dynamic state variable $K[t]$ to approximate the effects of potassium currents.

Voltage- and Experience-Dependent Potassium Current.

We define a conductance state variable $K^l[t]$ to model the dynamics of the neuron's total potassium current. Before reaching the spike threshold, $K^l[t]$ evolves according to both membrane potential and its activation history:

$$K^l[t] = \alpha K^l[t - 1] + \beta U^l[t] \quad (12)$$

Here, α is the decay factor determining the proportion of potassium current preserved from the previous time step $t - 1$. The term $\beta U^l[t]$ represents the fast voltage-dependent activation of low-threshold potassium currents.

Potassium currents exhibit a surge during spiking, reminiscent of delayed rectifier or high-threshold activated potassium currents. This is incorporated by updating $K^l[t]$ with the spike output $S^l[t]$:

$$K^l[t] = K^l[t] + S^l[t] \quad (13)$$

The linear coupling of $K^l[t]$ with $U^l[t]$ creates a negative feedback loop and serves as the short-term memory to adaptively modulate neuronal excitability before the membrane potential reaches the spike threshold. The coupling of $K^l[t]$ to $S^l[t]$ models the explosive opening of potassium channels during spiking, which serves two distinct functions:

1. **Rapid repolarization of the membrane potential**, inducing a refractory period immediately after a spike.
2. **Slow decay of hyperpolarization**, as the elevated potassium conductance persists across time steps, with a fraction α preserved. This persistence makes $K^l[t]$ a strong proxy for long-term spiking experience, integrating both recent and historical activity into excitability regulation.

Shunting Synaptic Inputs. In biological neurons, synaptic inputs are typically received on dendrites, where local potassium channels can shunt the postsynaptic response, reducing excitatory drive. Given the absence of dendritic compartments in our model, we simulate this process by modulating the postsynaptic current $I^l[t]$ using the potassium channel state variable from the previous time step:

$$I^l[t] = I^l[t] \odot (1 - \gamma\sigma(K^l[t-1])) \quad (14)$$

Here, $\sigma(\cdot)$ denotes the sigmoid function, which maps the potassium current to a normalized activation probability, and γ scales the magnitude of the shunting effect. The term $(1 - \gamma \cdot \sigma(K^l[t-1]))$ functions as a dynamic shunting gate, decreasing the strength of input currents. This conductance-based gating mechanism regulates neuronal excitability during the subthreshold integration phase, slowing depolarization, preventing excessive spiking, and enhancing overall network stability.

Potassium Channels for Adaptive Repolarization. To simulate somatic repolarization dynamics, we implement an adaptive reset mechanism that mimics biological after-hyperpolarization. In the KvLIF model, the membrane potential is updated as:

$$U^l[t] = U^l[t] - S^l[t] \odot (V_{th} + \sigma(K^l[t])) \quad (15)$$

The reset depth here is dynamically modulated by $\sigma(K^l[t])$. Since $K^l[t]$ surges immediately upon spiking, this term forces the membrane potential to drop significantly below the resting membrane potential. Larger $K^l[t]$ values result

Algorithm 1 Core computation of the KvLIF model

Input: Input current I , time step t , previous membrane potential U_{pre} , previous state variable K_{pre} .

Hyperparameters: Decay constant λ , threshold V_{th} , Potassium current decay factor α , membrane potential scaling factor β , shunting effect scaling factor γ .

Output: Spike S

```

1: if  $t = 0$  then
2:   Set  $U_{pre} \leftarrow 0$  and  $K_{pre} \leftarrow 0$            ▷ initialization
3: end if
4:  $I \leftarrow I \odot (1 - \gamma\sigma(K_{pre}))$            ▷ Shunting synaptic inputs
5:  $U \leftarrow \lambda U_{pre} + I$                        ▷ leaky & integrate
6:  $K_{init} \leftarrow \alpha K_{pre} + \beta U$            ▷ Potassium currents
7:  $S \leftarrow H(U - V_{th})$                          ▷ fire
8:  $K \leftarrow K_{init} + S$                            ▷ Potassium currents surge
9:  $U \leftarrow U - S \odot V_{th}$                        ▷ reset
10:  $U \leftarrow U - S \odot \sigma(K)$                  ▷ Adaptive repolarization.
    
```

Return S

in deeper resets, effectively extending the relative refractory period. This induces spike-frequency adaptation, thereby stabilizing network activity.

Building upon these foundational principles, we derive the KvLIF model as:

$$\begin{aligned}
 U^l[t] &= \lambda U^l[t-1] + I^l[t] \odot (1 - \gamma\sigma(K^l[t-1])) \\
 S^l[t] &= H(U^l[t] - V_{th}) \\
 K^l[t] &= \alpha K^l[t-1] + \beta U^l[t] + S^l[t] \\
 U^l[t] &= U^l[t] - S^l[t] \odot (V_{th} + \sigma(K^l[t]))
 \end{aligned} \quad (16)$$

The pseudo-code for KvLIF (Algorithm 1) outlines the sequence of operations, illustrating how the potassium current state variable interacts with the membrane potential and preceding spiking history. Functioning as a dual-phase regulator, $K^l[t]$ modulates subthreshold depolarization through A-type potassium current-like mechanisms and controls repolarization depth via delayed rectifier potassium current-like mechanisms. This integrated regulation ensures that the integration and reset phases remain precisely coordinated at every time step.

Overall, by adaptively modulating membrane dynamics using both real-time voltage and accumulated spiking experience, KvLIF offers several computational advantages over the LIF model, including extended dynamic range, improved noise robustness, enhanced temporal adaptability, and greater biological plausibility.

4.3. Dynamic Analysis of the KvLIF Model

To evaluate the self-adaptation capabilities of the proposed KvLIF neuron, we compare its dynamic response with that of conventional LIF neuron models. As shown in Figure

Table 1. Performance comparison with existing methods on static image datasets.

Dataset	Method	Network Architecture	Timestep	Accuracy (%)
CIFAR10	Dspike (Li et al., 2021)	Modified ResNet-18	4 / 6	93.66 / 94.05
	DSR (Meng et al., 2022)	PreAct-ResNet-18	20	95.40
	GLIF (Yao et al., 2022)	ResNet-18	4 / 6	94.64 / 94.88
	SML (Deng et al., 2023)	ResNet-18	4 / 6	95.01 / 95.12
	CLIF (Huang et al., 2024)	ResNet-18	4 / 6	94.89 / 95.41
	ILIF (Sun et al., 2025)	ResNet-18	4 / 6	95.24 / 95.49
	KvLIF (Ours)	ResNet-18	4 / 6	95.28 / 95.55
	Temporal Pruning (Chowdhury et al., 2022)	VGG-16	5	93.90
	ILIF (Sun et al., 2025)	VGG-16	6	94.25
	KvLIF (Ours)	VGG-16	6	94.36
CIFAR100	Dspike (Li et al., 2021)	Modified ResNet-18	4 / 6	73.35 / 74.24
	DSR (Meng et al., 2022)	PreAct-ResNet-18	20	78.50
	GLIF (Yao et al., 2022)	ResNet-18	4 / 6	76.42 / 77.28
	SML (Deng et al., 2023)	ResNet-18	4 / 6	77.36 / 78.00
	CLIF (Huang et al., 2024)	ResNet-18	4 / 6	77.00 / 78.36
	ILIF (Sun et al., 2025)	ResNet-18	4 / 6	77.43 / 78.51
	KvLIF (Ours)	ResNet-18	4 / 6	77.76 / 79.30
	Temporal Pruning (Chowdhury et al., 2022)	VGG-16	5	71.58
	ILIF (Sun et al., 2025)	VGG-16	6	75.25
	KvLIF (Ours)	VGG-16	6	76.13
TinyImageNet	Joint A-SNN (Guo et al., 2023)	VGG-16	4	55.39
	ASGL (Wang et al., 2023)	VGG-13	4 / 8	56.57 / 56.81
	CLIF (Huang et al., 2024)	VGG-13	4 / 6	63.16 / 64.13
	CPT-SNN (Xia et al., 2025)	VGG-13	4 / 8	63.39 / 64.78
	KvLIF (Ours)	VGG-13	4 / 6	64.03 / 64.82

3, all models are subjected to identical Poisson input spike trains over 40 time steps.

Regulation of Neuronal Excitability. Both conventional LIF models exhibit high firing rates, indicating a general tendency toward over-excitability. In contrast, the KvLIF neuron regulates its firing to a lower rate of 17.50%, reflecting efficient self-adaptation that suppresses redundant spikes.

Post-spike Membrane Dynamics. In the soft-reset LIF, high post-spike residual potentials cause hypersensitivity to subsequent inputs (Figure 3, middle). The hard-reset LIF model forces the potential to the resting state, erasing the membrane potential history. The KvLIF neuron exhibits an after-hyperpolarization phase, where the potential drops significantly below the resting potential (Figure 3, right column). By incorporating the negative feedback mechanism, the KvLIF model naturally inhibits excessive spiking, thereby enhancing the flexibility for encoding complex temporal patterns.

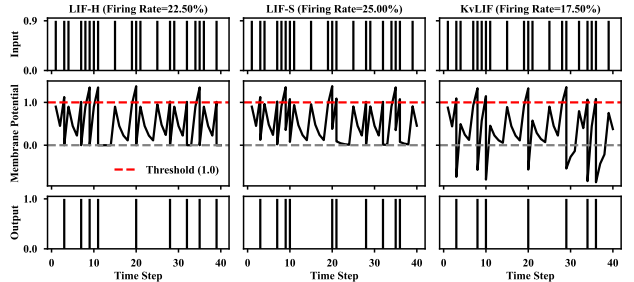


Figure 3. Comparison of dynamic responses between the KvLIF model and two conventional LIF models.

4.4. Stability and Adaptability Analysis of the KvLIF model

The improved stability of the KvLIF model is illustrated in Figure 4(a). By analyzing layer-wise gradient L2 norms, we observe that KvLIF model achieves more stable gradient propagation, as evidenced by a lower standard deviation compared to conventional LIF models. Figure 4(b) further demonstrates the model’s enhanced adaptability: KvLIF model attains over 90% accuracy in just one time step,

Table 2. Performance comparison with existing methods on neuromorphic datasets. The asterisk (*) denotes implementations achieved solely by modifying neuron models within the open source code (Huang et al., 2025).

Dataset	Method	Network Architecture	Timestep	Accuracy (%)
CIFAR10-DVS	Dspike (Li et al., 2021)	ResNet-18	10	75.40
	PLIF (Fang et al., 2021)	PLIF-Net	20	74.80
	GLIF (Yao et al., 2022)	7B-wideNet	16	78.10
	CLIF (Huang et al., 2024)	VGG-11	16	79.00
	ILIF (Sun et al., 2025)	VGG-11	10	78.60
	KvLIF (Ours)	VGG-11	10	79.50
	PSN (Fang et al., 2023b)	VGGSNN	10	85.90
	CLIF (Huang et al., 2024)	VGGSNN	10	86.10
	AR-LIF (Huang et al., 2025)	VGGSNN	16	87.90
	KvLIF (Ours)*	VGGSNN	10	88.40
DVS-Gesture	PLIF (Fang et al., 2021)	PLIF-Net	20	97.57
	KLIF (Jiang & Zhang, 2024)	Modified PLIF Net	12	94.10
	CLIF (Huang et al., 2024)	VGG-11	20	97.92
	AGMM (Liang et al., 2025)	VGGSNN	16	97.92
	ILIF (Sun et al., 2025)	VGG-11	20	97.92
	KvLIF (Ours)	VGG-11	10	98.26

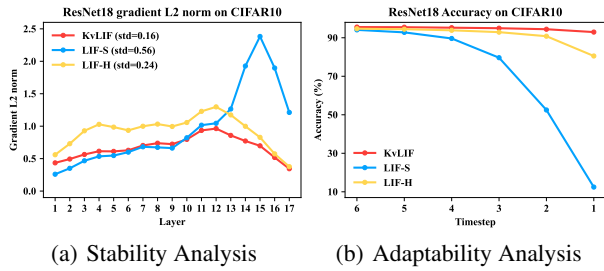


Figure 4. Comparative performance of KvLIF and conventional LIF models. (a) Gradient L2 norm distribution. (b) Performance retention as inference time steps reduce.

confirming its ability to perform adaptive encoding and enabling efficient inference within shorter time windows. This capability is further validated through experiments on neuromorphic datasets (Section 5.2).

5. Experiments

We conduct a series of experiments to evaluate the proposed KvLIF neuron model, with all details provided in the Appendix B.

5.1. Performance Comparison

To evaluate the effectiveness of the proposed KvLIF neuron model in SNN, we compare it with other neuron models and SNN methods. The comparisons with conventional LIF models are provided in the Appendix C. Our experiments span both static image and neuromorphic datasets across different network architectures. To faithfully unveil

Table 3. Robustness test on CIFAR100 under different noise levels.

Neuron	0.04	0.08	0.12	0.16	0.20
LIF-S	65.58	53.96	40.81	29.74	21.57
LIF-H	71.60	61.23	44.35	30.57	21.33
GLIF	69.71	62.38	50.40	38.19	28.05
CLIF	75.57	66.71	60.71	40.83	29.93
ILIF	74.52	65.33	50.24	36.49	25.44
KvLIF	76.10	68.37	63.03	44.27	33.32

Table 4. Robustness test on DVS-Gesture under different noise levels.

Neuron	0.10	0.20	0.30	0.40	0.50
LIF-S	90.63	84.03	77.78	69.10	66.32
LIF-H	77.78	68.40	60.07	55.56	52.08
GLIF	79.86	79.86	77.08	67.36	58.68
CLIF	89.58	82.64	75.69	63.89	57.29
ILIF	86.46	76.74	70.83	61.46	56.25
KvLIF	93.75	89.93	86.11	80.90	75.69

the improved performance due to the proposed method, we exclude other advanced data augmentation techniques like AutoAugment and CutMix, utilizing only standard preprocessing.

As shown in Table 1, the KvLIF model consistently achieves the highest accuracy on static image datasets across multiple network architectures. Using Spiking Resnet-18 with six time steps, KvLIF attains 95.55% accuracy on CIFAR10

Table 5. Ablation study of the proposed KvLIF neuron on different datasets.

Settings		CIFAR10	CIFAR100	Tiny-ImageNet	CIFAR10-DVS	DVS-Gesture
Shunting Synaptic Inputs	Adaptive Repolarization					
✓	✓	95.55	79.30	64.82	79.50	98.26
✗	✓	95.46	79.22	64.23	78.60	97.57
✓	✗	94.26	77.43	62.82	77.60	97.22
✗	✗	94.09	77.05	62.70	77.20	96.18

and 79.30% on CIFAR100. On the larger Tiny-ImageNet dataset, with Spiking VGG-13 (six time steps), it achieves 64.82% accuracy.

The proposed KvLIF model also exhibits strong performance in processing asynchronous spatiotemporal information. We evaluate it on two neuromorphic datasets, CIFAR10-DVS (Li et al., 2017) and DVS-Gesture (Amir et al., 2017), with results summarized in Table 2. On CIFAR10-DVS, KvLIF achieves 79.50% accuracy using Spiking VGG-11 with ten time steps, and 88.40% with VGGSNN. On DVS-Gesture, it attains 98.26% accuracy with Spiking VGG-11 (ten time steps). Notably, in most cases KvLIF achieves higher accuracy on both datasets with fewer time steps than competing methods, highlighting its advantage in handling complex spatiotemporal information.

Moreover, KvLIF achieves a lower firing rate and exhibits energy consumption comparable to the conventional LIF models (Appendix D and E).

5.2. Robustness Analysis

The adaptive regulation of neuronal excitability in KvLIF also enhances robustness to noise perturbations. For static image datasets, we utilize the Spiking ResNet-18 architecture and add Gaussian noise to the test set, sampled from a zero-mean Gaussian distribution with standard deviations ranging from 0.04 to 0.20. For neuromorphic datasets, we employ the Spiking VGG-11 architecture. To preserve the data sparsity, noise is added to 10%–50% of randomly selected pixels in the test set. Results for CIFAR100 and DVS-Gesture are presented in Tables 3 and 4, with additional robustness evaluations on other datasets provided in the Appendix (Tables 9 and 10, Appendix F).

In static image experiments, classification accuracy decreases for all models as noise increases. However, the KvLIF model consistently outperforms other neuron models across all noise levels. Similarly, in neuromorphic experiments, all models exhibit reduced accuracy with increasing proportions of added Gaussian noise, but KvLIF maintains the highest accuracy at all levels, demonstrating strong resilience to event noise.

These findings confirm that adaptive regulation in KvLIF

provides consistent robustness, effectively mitigating spatial perturbations in static images and event noise in neuromorphic data streams.

Additionally, the model demonstrates robustness to missing temporal events, attributed to the improved adaptability of the KvLIF model (Tables 11 and 12, Appendix G).

5.3. Ablation Study

We analyze the relative contributions of the two adaptive components in the KvLIF model: the A-type current, which integrates membrane potential to shunt synaptic inputs, and the delayed rectifier current, which accumulates spiking history to regulate post-spike reset dynamics. Detailed quantitative results are presented in Table 5. Adaptive repolarization plays a more significant role in the improved performance of KvLIF, with its ablation causing a larger performance drop across all tested datasets. In comparison, synaptic shunting has a smaller impact.

6. Conclusion

In this study, we address key limitations of conventional LIF models, namely their restricted dynamic range and susceptibility to noise, which hinder adaptability in complex environments. To overcome these challenges, we propose the KvLIF model, inspired by the self-regulatory voltage-gated potassium channels. The A-type potassium current modulates subthreshold integration, while the delayed rectifier potassium current regulates post-spike reset, enabling the model to extend its signal representation range and suppress noise-induced spikes. Extensive evaluations on static and neuromorphic image datasets demonstrate that the KvLIF model consistently achieves superior classification accuracy and robustness compared to existing models. Overall, this work introduces a powerful LIF variant for SNN research and shows that integrating biological plausibility with computational efficiency is an effective strategy for building robust, energy-efficient SNNs.

Impact Statement

This work bridges biophysical principles and efficient model design, demonstrating how biologically inspired self-regulation can create more robust and adaptable SNNs. By improving noise resilience and dynamic range, it directly contributes to the development of reliable and energy-efficient neuromorphic computing for real-world applications like edge AI and autonomous systems.

References

- Amir, A., Taba, B., Berg, D., Melano, T., McKinstry, J., Di Nolfo, C., Nayak, T., Andreopoulos, A., Garreau, G., Mendoza, M., Kusnitz, J., Debole, M., Esser, S., Delbruck, T., Flickner, M., and Modha, D. A low power, fully event-based gesture recognition system. In *2017 IEEE Conference on Computer Vision and Pattern Recognition (CVPR)*, pp. 7388–7397, 2017.
- Bean, B. P. The action potential in mammalian central neurons. *Nature Reviews Neuroscience*, 8(6):451–465, 2007.
- Benda, J. and Herz, A. V. A universal model for spike-frequency adaptation. *Neural computation*, 15(11):2523–2564, 2003.
- Chowdhury, S. S., Rathi, N., and Roy, K. Towards ultra low latency spiking neural networks for vision and sequential tasks using temporal pruning. In *European Conference on Computer Vision*, pp. 709–726, 2022.
- Connor, J. and Stevens, C. Prediction of repetitive firing behaviour from voltage clamp data on an isolated neurone soma. *The Journal of physiology*, 213(1):31, 1971.
- Deng, S., Li, Y., Zhang, S., and Gu, S. Temporal efficient training of spiking neural network via gradient re-weighting. In *International Conference on Learning Representations*, 2022.
- Deng, S., Lin, H., Li, Y., and Gu, S. Surrogate module learning: Reduce the gradient error accumulation in training spiking neural networks. In *International Conference on Machine Learning*, pp. 7645–7657, 2023.
- Eshraghian, J. K., Ward, M., Neftci, E. O., Wang, X., Lenz, G., Dwivedi, G., Bennamoun, M., Jeong, D. S., and Lu, W. D. Training spiking neural networks using lessons from deep learning. *Proceedings of the IEEE*, 111(9): 1016–1054, 2023.
- Fang, W., Yu, Z., Chen, Y., Masquelier, T., Huang, T., and Tian, Y. Incorporating learnable membrane time constant to enhance learning of spiking neural networks. In *Proceedings of the IEEE/CVF international conference on computer vision*, pp. 2661–2671, 2021.
- Fang, W., Chen, Y., Ding, J., Yu, Z., Masquelier, T., Chen, D., Huang, L., Zhou, H., Li, G., and Tian, Y. Spikingjelly: An open-source machine learning infrastructure platform for spike-based intelligence. *Science Advances*, 9(40): eadi1480, 2023a.
- Fang, W., Yu, Z., Zhou, Z., Chen, D., Chen, Y., Ma, Z., Masquelier, T., and Tian, Y. Parallel spiking neurons with high efficiency and ability to learn long-term dependencies. In *Advances in Neural Information Processing Systems*, volume 36, pp. 53674–53687, 2023b.
- Fitz, H., Uhlmann, M., Van den Broek, D., Duarte, R., Hagoort, P., and Petersson, K. M. Neuronal spike-rate adaptation supports working memory in language processing. *Proceedings of the National Academy of Sciences*, 117(34):20881–20889, 2020.
- Gerstner, W. and Kistler, W. M. *Spiking Neuron Models: Single Neurons, Populations, Plasticity*. Cambridge University Press, 2002.
- Gerstner, W., Kistler, W. M., Naud, R., and Paninski, L. *Neuronal dynamics: From single neurons to networks and models of cognition*. Cambridge University Press, 2014.
- Guo, Y., Chen, Y., Zhang, L., Wang, Y., Liu, X., Tong, X., Ou, Y., Huang, X., and Ma, Z. Reducing information loss for spiking neural networks. In *European Conference on Computer Vision*, pp. 36–52, 2022.
- Guo, Y., Peng, W., Chen, Y., Zhang, L., Liu, X., Huang, X., and Ma, Z. Joint a-snn: Joint training of artificial and spiking neural networks via self-distillation and weight factorization. *Pattern Recognition*, 142:109639, 2023.
- Han, S., Pool, J., Tran, J., and Dally, W. Learning both weights and connections for efficient neural network. In *Advances in Neural Information Processing Systems*, volume 28, 2015.
- Huang, Y., Lin, X., Ren, H., Fu, H., Zhou, Y., Liu, Z., Pan, B., and Cheng, B. Clif: Complementary leaky integrate-and-fire neuron for spiking neural networks. In *Proceedings of the 41st International Conference on Machine Learning*, volume 235, pp. 19949–19972, 2024.
- Huang, Z., Meng, W., Liu, Q., Chen, K., and Ma, L. Ar-lif: Adaptive reset leaky integrate-and-fire neuron for spiking neural networks. *arXiv preprint arXiv:2507.20746*, 2025.
- Jiang, C. and Zhang, Y. Klif: An optimized spiking neuron unit for tuning surrogate gradient function. *Neural Computation*, 36(12):2636–2650, 2024.
- Li, H., Liu, H., Ji, X., Li, G., and Shi, L. Cifar10-dvs: an event-stream dataset for object classification. *Frontiers in neuroscience*, 11:244131, 2017.

- Li, Y., Guo, Y., Zhang, S., Deng, S., Hai, Y., and Gu, S. Differentiable spike: Rethinking gradient-descent for training spiking neural networks. In *Advances in neural information processing systems*, volume 34, pp. 23426–23439, 2021.
- Liang, Y., Wei, W., Belatreche, A., Cao, H., Zhou, Z., Wang, S., Zhang, M., and Yang, Y. Towards accurate binary spiking neural networks: Learning with adaptive gradient modulation mechanism. In *Proceedings of the AAAI Conference on Artificial Intelligence*, volume 39, pp. 1402–1410, 2025.
- Maass, W. Networks of spiking neurons: The third generation of neural network models. *Neural Networks*, 10(9): 1659–1671, 1997.
- Meng, Q., Xiao, M., Yan, S., Wang, Y., Lin, Z., and Luo, Z.-Q. Training high-performance low-latency spiking neural networks by differentiation on spike representation. In *Proceedings of the IEEE/CVF conference on computer vision and pattern recognition*, pp. 12444–12453, 2022.
- Rathi, N. and Roy, K. Diet-snn: A low-latency spiking neural network with direct input encoding and leakage and threshold optimization. *IEEE Transactions on Neural Networks and Learning Systems*, 34(6):3174–3182, 2021.
- Schuman, C. D., Kulkarni, S. R., Parsa, M., Mitchell, J. P., Date, P., and Kay, B. Opportunities for neuromorphic computing algorithms and applications. *Nature Computational Science*, 2(1):10–19, 2022.
- Sun, K., Duan, P., Kuhlmann, L., Wang, B., and Zhang, B. Ilif: Temporal inhibitory leaky integrate-and-fire neuron for overactivation in spiking neural networks. In *Proceedings of the Thirty-Fourth International Joint Conference on Artificial Intelligence, IJCAI-25*, pp. 4200–4208, 2025.
- Vacher, H., Mohapatra, D. P., and Trimmer, J. S. Localization and targeting of voltage-dependent ion channels in mammalian central neurons. *Physiological reviews*, 88(4):1407–1447, 2008.
- Wang, L. and Yu, Z. Autaptic synaptic circuit enhances spatio-temporal predictive learning of spiking neural networks. In *Proceedings of the 41st International Conference on Machine Learning*, volume 235, pp. 52083–52098, 2024.
- Wang, S., Cheng, T. H., and Lim, M.-H. Ltmd: learning improvement of spiking neural networks with learnable thresholding neurons and moderate dropout. In *Advances in Neural Information Processing Systems*, volume 35, pp. 28350–28362, 2022.
- Wang, Z., Jiang, R., Lian, S., Yan, R., and Tang, H. Adaptive smoothing gradient learning for spiking neural networks. In *Proceedings of the 40th International Conference on Machine Learning*, volume 202, pp. 35798–35816, 2023.
- Werbos, P. J. Backpropagation through time: what it does and how to do it. *Proceedings of the IEEE*, 78(10):1550–1560, 2002.
- Wu, Y., Deng, L., Li, G., Zhu, J., and Shi, L. Spatio-temporal backpropagation for training high-performance spiking neural networks. *Frontiers in neuroscience*, 12: 331, 2018.
- Xia, Q., Yu, Y., Chang, Z., Hui, B., and Luo, H. Cpt-snn: A spiking neural network that can combine the previous timestep. *Neurocomputing*, pp. 130253, 2025.
- Yao, M., Hu, J., Zhou, Z., Yuan, L., Tian, Y., Xu, B., and Li, G. Spike-driven transformer. In *Advances in Neural Information Processing Systems*, volume 36, pp. 64043–64058, 2023.
- Yao, X., Li, F., Mo, Z., and Cheng, J. Glif: A unified gated leaky integrate-and-fire neuron for spiking neural networks. In *Advances in Neural Information Processing Systems*, volume 35, pp. 32160–32171, 2022.
- Zang, Y., Hong, S., and De Schutter, E. Firing rate-dependent phase responses of purkinje cells support transient oscillations. *Elife*, 9:e60692, 2020.
- Zang, Y., Marder, E., and Marom, S. Sodium channel slow inactivation normalizes firing in axons with uneven conductance distributions. *Current biology*, 33(9):1818–1824, 2023.
- Zenke, F. and Ganguli, S. Superspike: Supervised learning in multilayer spiking neural networks. *Neural computation*, 30(6):1514–1541, 2018.
- Zhang, S., Yang, Q., Ma, C., Wu, J., Li, H., and Tan, K. C. Tc-lif: A two-compartment spiking neuron model for long-term sequential modelling. In *Proceedings of the AAAI conference on artificial intelligence*, volume 38, pp. 16838–16847, 2024.

A. Visualization of Feature Maps

We visualize the feature maps of the encoding layer in the LIF-based ResNet-18 on CIFAR10, as shown in Figure 5. Observations reveal that the input intensities received by LIF neurons significantly exceed 1.0, confirming that these neurons indeed process high-intensity signals.

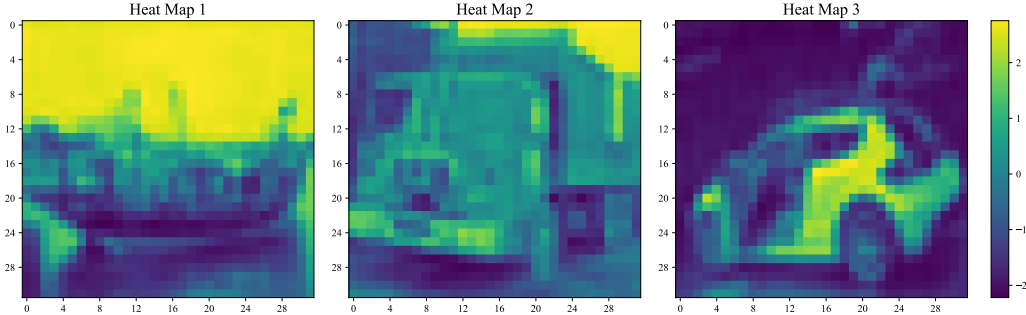


Figure 5. Heatmap visualization of the encoding layer responses to different input samples.

B. Detailed Experimental Settings and Dataset Preprocessing

All experiments are conducted under a consistent configuration unless otherwise specified. We employ the Rectangle surrogate gradient function with $\sigma = V_{th} = 1$ and set the decay constant to 0.5. The random seed is fixed at 1000 for all runs. For the loss function, we utilize the TET method with a lambda value of 0.05 (Deng et al., 2022). Detailed training hyperparameters are listed in Table 6.

Table 6. Training hyperparameter settings for various datasets.

Dataset	Bacth Size	Epoch	Learning Rate	Optimizer	Weight Decay	α	β	γ
CIFAR10	128	200	0.1	SGD	5e-5	0.8	0.3	0.05
CIFAR100	128	300	0.1	SGD	5e-4	0.8	0.1	0.05
Tiny-ImageNet	256	300	0.1	SGD	5e-4	0.8	0.3	0.05
CIFAR10-DVS	128	200	0.05	SGD	5e-4	0.8	0.1	0.05
DVS-Gesture	16	150	5e-4	Adam	0.0	0.8	0.3	0.05

CIFAR10 and CIFAR100. These datasets each contain 60,000 color images (32×32 pixels), divided into 50,000 training and 10,000 testing samples across 10 and 100 classes, respectively. Data preprocessing includes random cropping with 4-pixel padding, random horizontal flipping, and Cutout. Image data are normalized to zero mean and unit variance. We employ the direct encoding method (Rathi & Roy, 2021), where pixel values are repeatedly input into the model at each time step. The backbone network for these tasks is Spiking ResNet-18.

Tiny-ImageNet. This dataset contains 100,000 color images (64×64 pixels) from 200 classes. Our preprocessing pipeline includes random cropping with 8-pixel padding and horizontal flipping. Direct encoding is utilized for input representation. The backbone network employed is Spiking VGG-13.

CIFAR10-DVS. This neuromorphic dataset comprises 10,000 event-driven samples derived from CIFAR-10, obtained by recording the original images using a Dynamic Vision Sensor (DVS) (Li et al., 2017). Each sample features an original spatial resolution of 128×128 pixels. Each sample is processed using event-to-frame integration, with the spatial resolution at each time step resized to 48×48 . This is followed by random cropping with 4-pixel padding to generate the final preprocessed samples. We adopt Spiking VGG-11 as the backbone network.

DVS-Gesture. This dataset captures 11 distinct hand gesture categories performed by 29 subjects under three different lighting conditions (Amir et al., 2017). It consists of 1,342 event-based samples (128×128 pixels), divided into 1,208 training and 134 testing samples. For preprocessing, we utilize the SpikingJelly framework to implement event-to-frame integration (Fang et al., 2023a). The backbone network employed is Spiking VGG-11.

C. Comparison with Conventional LIF models

To evaluate the effectiveness of the proposed KvLIF neuron, we compare it with conventional LIF models on both static and neuromorphic datasets, as summarized in Table 7. The experiments cover multiple network architectures and timesteps, assessing the model’s generalization ability under different input modalities.

Experimental results indicate that the KvLIF model delivers consistently better classification accuracy than the baseline models on all evaluated datasets and network architectures. KvLIF consistently excels on static datasets at both $T = 4$ and $T = 6$, particularly on the challenging Tiny-ImageNet ($T = 6$) where it achieves 64.82%, significantly surpassing conventional LIF models. Regarding neuromorphic tasks, the model demonstrates superior temporal processing, attaining peak accuracies of 79.30% on CIFAR10-DVS and 98.26% on DVS-Gesture. The enhanced representational ability provided by KvLIF directly yields superior performance across a wide range of tasks.

Table 7. Performance comparison with conventional LIF models.

Dataset	Architecture	Neuron	Timestep	Accuracy (%)
CIFAR10	ResNet-18	LIF-S	4 / 6	91.54 / 94.09
	ResNet-18	LIF-H	4 / 6	94.42 / 94.70
	ResNet-18	KvLIF	4 / 6	95.28 / 95.55
CIFAR100	ResNet-18	LIF-S	4 / 6	69.24 / 77.05
	ResNet-18	LIF-H	4 / 6	74.64 / 77.17
	ResNet-18	KvLIF	4 / 6	77.76 / 79.30
Tiny-ImageNet	VGG-13	LIF-S	4 / 6	60.72 / 62.70
	VGG-13	LIF-H	4 / 6	61.58 / 61.81
	VGG-13	KvLIF	4 / 6	64.03 / 64.82
CIFAR10-DVS	VGG-11	LIF-S	10	77.20
	VGG-11	LIF-H	10	77.90
	VGG-11	KvLIF	10	79.30
DVS-Gesture	VGG-11	LIF-S	10	96.18
	VGG-11	LIF-H	10	96.88
	VGG-11	KvLIF	10	98.26

Table 8. The energy consumption of synaptic operation on different datasets.

Dataset	Architecture	Neuron	T	ACs (M)	MACs (M)	SOP Energy (μ J)
CIFAR10	ResNet-18	ReLU	1	0.00	549.13	2526.00
	ResNet-18	LIF-S	6	512.82	3.34	476.91
	ResNet-18	LIF-H	6	487.93	3.34	454.51
	ResNet-18	KvLIF	6	393.16	13.37	415.34
CIFAR100	ResNet-18	ReLU	1	0.00	549.18	2526.22
	ResNet-18	LIF-S	6	359.34	3.34	338.78
	ResNet-18	LIF-H	6	404.70	3.34	379.61
	ResNet-18	KvLIF	6	320.60	13.37	350.05
Tiny-ImageNet	VGG-13	ReLU	1	0.00	913.46	4201.90
	VGG-13	LIF-S	6	885.85	6.00	824.86
	VGG-13	LIF-H	6	822.80	6.00	768.11
	VGG-13	KvLIF	6	679.14	23.99	721.58
DVS-Gesture	VGG-11	LIF-S	10	3674.48	24.25	3418.58
	VGG-11	LIF-H	10	2992.54	24.25	2804.83
	VGG-11	KvLIF	10	2503.10	96.99	2698.96
CIFAR10-DVS	VGG-11	LIF-S	10	302.70	3.41	288.15
	VGG-11	LIF-H	10	264.66	3.41	253.88
	VGG-11	KvLIF	10	241.49	13.64	280.12

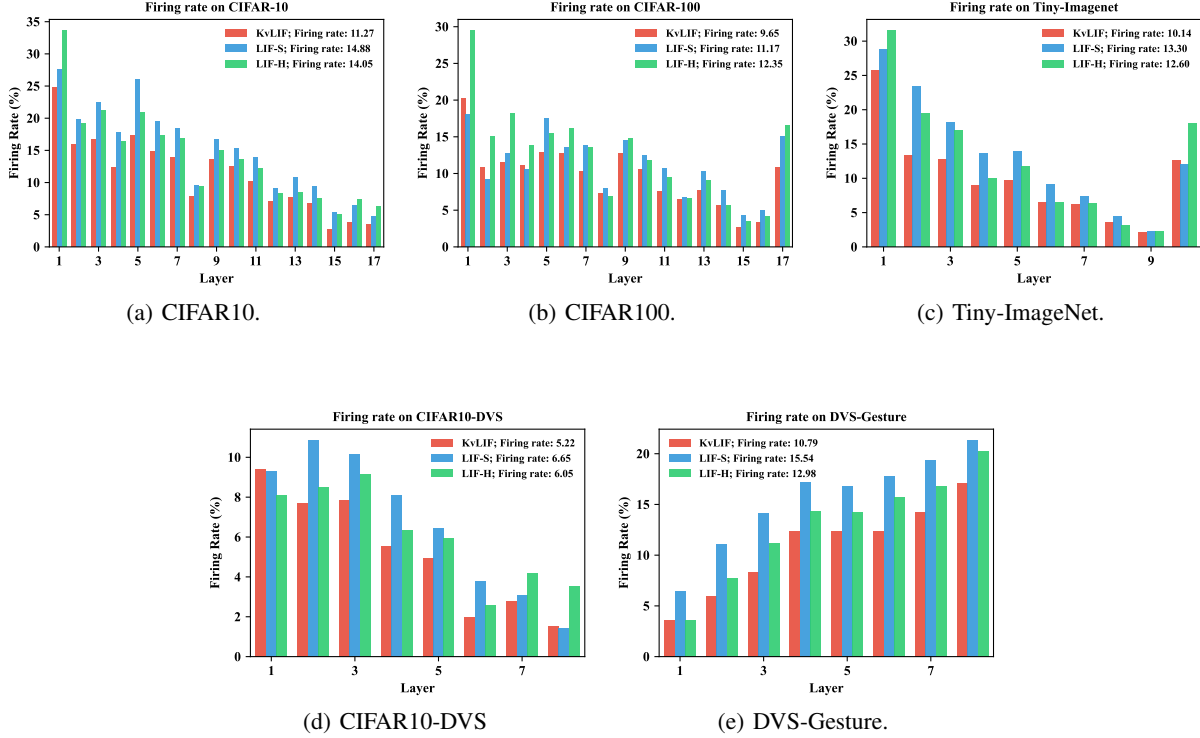


Figure 6. Firing rate comparison across different datasets.

D. Firing Rate Analysis

We calculate the layer-wise firing rates of KvLIF compared to conventional LIF models across five datasets, as shown in Figure 6. The results demonstrate that KvLIF consistently achieves lower firing rates on both static image datasets (CIFAR10, CIFAR100, Tiny-ImageNet) and neuromorphic datasets (CIFAR10-DVS, DVS-Gesture). This significant reduction in spiking activity is attributed to the intrinsic adaptive mechanism of the KvLIF neuron. By effectively suppressing the generation of redundant spikes, KvLIF ensures that only task-relevant information is transmitted, thereby maximizing computational sparsity.

E. Energy Consumption Analysis

To evaluate the energy efficiency of the proposed model, we analyze the total energy consumption based on Synaptic Operations (SOP) (Yao et al., 2023). The total energy consumption is calculated by summing the accumulation (AC) and multiply-accumulate (MAC) operations, weighted by their respective unit energy costs. The formulation is given by:

$$SOP = E_{AC} \cdot N_{AC} + E_{MAC} \cdot N_{MAC}, \quad (17)$$

where E_{AC} and E_{MAC} denote the energy cost per operation, and N_{AC} and N_{MAC} represent the total number of AC and MAC operations, respectively. Following established energy models in neuromorphic computing, we set E_{AC} to 0.9 pJ for one 32-bit floating-point AC and E_{MAC} to 4.6 pJ for one 32-bit floating-point MAC operation (Han et al., 2015).

As shown in Table 8, KvLIF maintains comparable or reduced energy consumption relative to conventional LIF models. The KvLIF model incurs an increase in MAC operations due to the additional updates required for potassium current dynamics. However, its significantly reduced spike firing rate effectively offsets this computational overhead, thereby preserving overall energy efficiency. These results fully demonstrate the effectiveness of incorporating potassium channel mechanisms for constructing energy-efficient and high-performance SNNs.

F. Additional Robustness Test

We conduct additional robustness tests on the static image dataset (CIFAR-10) and the neuromorphic dataset (CIFAR10-DVS). The noise settings follow the protocols described in Section 5.2 of the main text, and the results are summarized in Tables 9 and 10.

In the static image experiments, accuracy naturally degrades for all models as noise intensity increases. The KvLIF model consistently achieves higher accuracy than other neuron models across almost all noise levels. The only exception is at the 0.08 noise level, where it is slightly surpassed by others. Similarly, in the neuromorphic experiments, while all models exhibit reduced accuracy with increasing noise proportions, KvLIF maintains the highest accuracy at all levels, demonstrating superior resilience to event noise.

Table 9. Robustness test on CIFAR10 under different noise levels.

Neuron	0.04	0.08	0.12	0.16	0.20
LIF-S	90.65	86.74	79.91	70.96	60.75
LIF-H	93.72	90.87	86.38	79.59	71.82
GLIF	93.64	91.48	87.92	82.05	74.97
CLIF	94.44	92.46	88.40	82.69	74.98
ILIF	94.31	92.96	88.77	83.63	76.61
KvLIF	94.84	92.73	89.12	84.12	77.02

Table 10. Robustness test on CIFAR10-DVS under different noise levels.

Neuron	0.10	0.20	0.30	0.40	0.50
LIF-S	75.20	73.80	69.30	65.30	58.80
LIF-H	75.90	74.70	69.20	66.30	61.20
GLIF	70.20	61.40	51.00	40.60	31.30
CLIF	75.40	73.20	69.60	66.10	60.30
ILIF	75.80	75.70	72.80	70.00	64.40
KvLIF	77.10	75.90	74.40	72.10	69.00

G. Temporal Robustness Analysis

To verify the temporal robustness of the proposed KvLIF, we introduce temporal noise by randomly masking out a certain percentage of event time steps in the test sets. These experiments are conducted on both the DVS-Gesture and CIFAR10-DVS datasets, with drop rates ranging from 0.1 to 0.5.

Table 11. Temporal Robustness test on DVS-Gesture under different noise levels.

Neuron	0.10	0.20	0.30	0.40	0.50
LIF-S	96.53	95.83	94.10	92.36	89.93
LIF-H	95.83	95.14	90.28	78.47	60.07
GLIF	95.83	96.18	96.18	94.79	93.06
CLIF	96.18	95.49	94.44	93.06	90.97
ILIF	96.86	96.53	94.44	92.01	88.54
KvLIF	97.22	96.53	96.53	95.83	94.10

While the accuracy of all models naturally declines as noise levels increase, the KvLIF model demonstrates stronger temporal robustness. Specifically, on the DVS-Gesture dataset, KvLIF maintains the highest accuracy across all drop rates (Table 11). Similarly, on CIFAR10-DVS, it outperforms competing models at all noise levels, with the sole exception of the 0.4 drop rate (Table 12).

Table 12. Temporal Robustness test on CIFAR10-DVS under different noise levels.

Neuron	0.10	0.20	0.30	0.40	0.50
LIF-S	75.40	74.10	71.50	66.60	55.10
LIF-H	77.40	76.00	74.00	71.40	61.60
GLIF	74.10	69.70	63.80	55.50	43.70
CLIF	77.90	76.30	74.10	68.50	57.70
ILIF	78.10	76.20	74.60	71.60	63.80
KvLIF	79.00	77.90	74.70	71.10	65.00

H. Code Availability

We will release the code for the KvLIF neuron model and associated experiments publicly following publication.